Editors' Suggestion

Analysis of real-space transport channels for electrons and holes in halide perovskites

Frederik Vonhoff,[1] Maximilian J. Schilcher,[1] David R. Reichman,[2] and David A. Egger[1,3,*]
[1]Physics Department, TUM School of Natural Sciences, Technical University of Munich, 85748 Garching, Germany
[2]Department of Chemistry, Columbia University, New York, New York 10027, USA
[3]Atomistic Modeling Center, Munich Data Science Institute, Technical University of Munich, 85748 Garching, Germany

(Received 26 May 2025; accepted 29 July 2025; published 2 September 2025)

Predicting and explaining charge carrier transport in halide perovskites is a formidable challenge because of the unusual vibrational and electron-phonon coupling properties of these materials. This study explores charge carrier transport in two prototypical halide perovskite materials, methylammonium lead tribromide ($MAPbBr_3$) and methylammonium lead triiodide ($MAPbI_3$), using a dynamic disorder model. Focusing on the role of real-space transport channels, we analyze temporal orbital occupations to assess the impact of material-specific on-site energy levels and spin-orbit coupling (SOC) strengths. Our findings reveal that both on-site energies and SOC magnitude significantly influence the orbital occupation dynamics, thereby affecting charge dispersal and carrier mobility. In particular, energy gaps across on-site levels and the halide SOC strength govern the filling of transport channels over time. This leads us to identify the $pp\pi$ channel as a critical bottleneck for charge transport and to provide insights into the differences between electron and hole transport across the two materials.

DOI: 10.1103/c4v6-kf43

I. INTRODUCTION

Halide perovskites (HaPs) are an interesting class of semiconducting materials for optoelectronic applications, such as solar cells and light-emitting devices [1–3]. The exceptional performance of HaPs in device applications stems from their advantageous optoelectronic properties [4–7]. Prototypical HaPs exhibit direct band gaps, almost ideal absorption features with sharp absorption edges [8], relatively low exciton binding energies [9], and long charge carrier diffusion lengths [10,11]. Furthermore, their ABX_3 stoichiometry allows for realizing multiple material compositions with tunable optoelectronic properties. For example, the fundamental band gap of HaPs can be modified via their ionic composition [5,6,12], which is critical for utilizing these materials in tandem solar cells.

The design of new HaP materials hinges on improving our microscopic understanding of charge carrier transport in these systems, as it is a foundational mechanism in all semiconductor devices. However, modeling transport in HaPs defies established textbook frameworks at the same time: Carrier mobilities exhibit power-law behavior, which is a key signature of bandlike transport reminiscent of classical inorganic semiconductors such as bulk Si and GaAs [13]. Simultaneously, however, carrier relaxation times in HaPs are ultrafast, and mean free paths are ultrashort [14], which is reminiscent of molecular semiconductors [15–18]. Related to this, these materials show strongly anharmonic vibrations that cause large fluctuations in their electronic properties and unusual optoelectronic behavior [19–31]. Predictive computational modeling of the carrier transport of such seemingly contradictory scenarios is challenging, especially because violations of the Mott-Ioffe-Regel criterion [32,33] prohibit using standard band-transport theories [14,16,17]. Specifically, when mean free paths of charge carriers approach or even drop below the wavelengths of their wave packets, perturbative treatment of carrier-lattice coupling is not sensible because bandlike quasiparticles are not well-defined anymore. Indeed, established frameworks employing simplified models of Fröhlich polarons in combination with the Boltzmann transport equation fail to predict experimentally measured transport characteristics [22], which is expected for the parameter regime of HaPs [17]. Development of new predictive models for charge transport in HaPs is therefore an important challenge for theory. Such models could generate microscopic understanding of carrier transport in HaPs and faster progress and development of design principles in the context of other materials families, including inorganic semiconductors such as oxides [34,35] and nitrides [36] as well as organic semiconductors [15,16,18,37–44].

To tackle the illustrated challenges of modeling carrier transport in HaPs, some of the authors proposed a dynamic disorder (DD) model [14,22,24]. This model incorporates vibrational anharmonicity via the use of molecular dynamics (MD), which is critical to capturing the pronounced vibrational anharmonicity. Transient localization of charge carriers accompanying the vibrational fluctuations [14,40,45] is modeled via a tight-binding (TB) Hamiltonian that explicitly depends on the atomic configurations obtained in MD. The TB model is parameterized from first principles with density functional theory (DFT) using the geometries from

*Contact author: david.egger@tum.de

Published by the American Physical Society under the terms of the Creative Commons Attribution 4.0 International license. Further distribution of this work must maintain attribution to the author(s) and the published article's title, journal citation, and DOI.

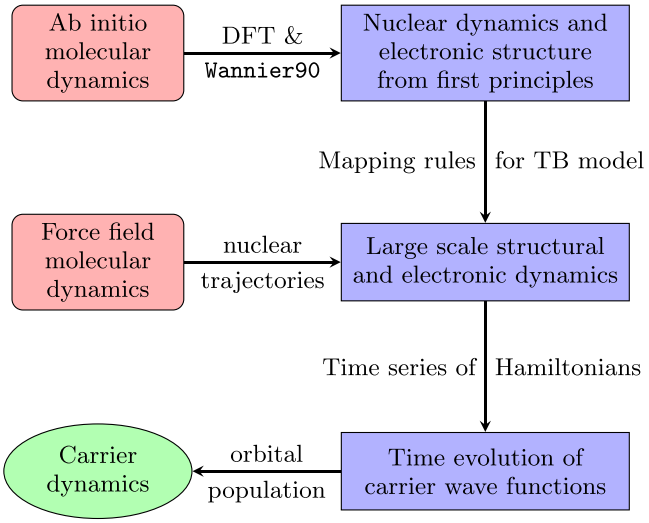


FIG. 1. Workflow of the dynamic disorder (DD) model: Each blue rectangular box represents one conceptual step in parametrizing the model and performing calculations with it; see text for details.

MD snapshots. The resulting time-dependent Hamiltonian allows one to predict the time evolution of electron (e^-) and hole (h^+) wave functions in the DD model. The computed carrier mobilities have been found to be in broad agreement with experiments with regard to magnitudes, temperature dependences, and chemical trends [22,24]. Notably, a recent experimental study provided evidence in support of the DD model, highlighting the crucial role of DD as the dominant scattering mechanism in HaPs [46].

In this study, we further develop the DD model to enable real-space analysis of carrier dynamics and investigate the consequences of using more accurate electronic-structure calculations to parametrize it. Using methylammonium lead tribromide ($MAPbBr_3$) and methylammonium lead triiodide ($MAPbI_3$) variants, we focus on how on-site energy levels and the magnitude of spin-orbit coupling (SOC), both determined by the chemical composition of the materials, interact with the dynamic fluctuations of the electronic structure in HaPs to produce the novel transport characteristics of these materials. To this end, we resolve time-dependent orbital occupations and elucidate the carrier-scattering mechanisms in three real-space transport channels that together determine carrier transport by either enhancing or suppressing mobility. By providing an in-depth analysis of transport channels in HaPs, this work enables an improved microscopic understanding of the foundational properties of these semiconducting materials.

II. METHODS

Figure 1 illustrates the workflow of the DD model developed in Refs. [22,24]. In brief, it involves three key steps: First, we sample the nuclear dynamics and electronic structure with *ab initio* MD to parametrize TB Hamiltonians. Second, TB Hamiltonians for large-scale structural and electronic dynamics are constructed. Third, carrier wave packets are evolved in time to monitor scattering effects due to nuclear dynamics and extract transport characteristics from it. We describe these three main steps in the following.

A. Nuclear dynamics and electronic structure from first principles

To parametrize the TB Hamiltonians, we create samples of the nuclear dynamics and electronic structures at finite temperature using *ab initio* MD. Specifically, we use data from Ref. [24], comprising MD trajectories spanning 35 ps for $MAPbI_3$ and $MAPbBr_3$ at 300 K in $2 \times 2 \times 2$ supercells. Extracting roughly 100 snapshots, we perform a DFT-based electronic-structure calculation using the Vienna Ab initio Simulation Package (VASP) [47] with the hybrid Heyd-Scuseria-Ernzerhof (HSE) functional using 25% Fock exchange [48,49] and incorporating SOC. Previous studies of the DD model [22,24] used the Perdew-Burke-Ernzerhof (PBE) functional [50], which captures the main features in electronic structures of HaPs but is less accurate than HSE [51,52].

The TB parameters for on-site energies, hoppings, and SOC are extracted via WANNIER90 [53] for Pb and X ions, using Pb s and p and halide X p atomic orbitals as the basis. The MA orbitals do not contribute significantly to the electronic structure close to the band gap, and therefore, we do not consider them explicitly when modeling charge transport. However, the dynamics of the MA molecule contribute to the DD of TB parameters, which we account for through MD and thereby capture its role in the transport. We denote on-site energies as ε_α^i, where i is the atomic index and α is the orbital index, and SOC parameters for X and Pb ions as γ_X and γ_{Pb}, respectively. We include the three hopping elements $t_{sp\sigma}$, $t_{pp\sigma}$, and $t_{pp\pi}$, which are indexed according to bonding type.

When hopping elements are plotted against interatomic Pb-X distances, we find that the HSE data broadly confirm previous PBE-based results [54]. The data show the expected exponential decrease with increasing distance, which can be fit by a function of the form $a\exp(-bx) + c$. This establishes a mapping rule between results from DFT calculations and TB parameters. We find that the fitting parameters b and c are similar for PBE and HSE calculations. However, the parameter a is significantly larger in the case of HSE compared to PBE data, which results in larger values for the hopping elements. For the on-site energies, the mapping is achieved via Ewald summations, where the computed parameters are shifted such that their mean values align with those calculated through DFT and WANNIER90 for $MAPbI_3$ and $MAPbBr_3$, respectively. The Ewald summation considers the structural environment of each atom in every MD snapshot separately, thereby accounting for the spatial and temporal fluctuations of the on-site energies as one source of DD. The SOC parameters for Pb and X ions are set to their respective mean values that we calculate with WANNIER90 across the MD trajectory since the temporal fluctuations are smaller than 3.5%. In summary, the extracted hopping elements, on-site energies, and SOC parameters are combined into a first-principles database, which provides a mapping rule to construct Hamiltonian matrices of large supercells depending on the time-dependent material geometries we extract from MD.

B. Large-scale structural and electronic dynamics

We construct Hamiltonian matrices for large supercells with the TB mapping rule parameterized from first principles. To model the structural dynamics at different temperatures, we use force field MD data from Ref. [24]. They contain $16 \times 16 \times 16$ supercells of $MAPbI_3$ and $MAPbBr_3$ at five different temperatures spanning 200 to 350 K, from which we extract 100 snapshots corresponding to 100 fs. The $16 \times 16 \times 16$ supercells are approximately 100 nm wide in each dimension and contain a total of 49 152 atoms. Using these snapshots, we obtain time series of Hamiltonians with the mapping rule using atomic distances as input and assigning on-site terms as well as SOC parameters as described before. To prevent finite-size effects, we periodically continue Hamiltonians of $16 \times 16 \times 16$ cells to $96 \times 96 \times 96$ cells.

C. Time evolution of carrier wave functions

We compute the time evolution of differently initialized wave functions from the large-scale structural and electronic dynamics. For initialization of e^- and h^+ carriers, we calculate the electronic Bloch eigenstates from the Hamiltonian of the first snapshot. These states are constructed from the primitive unit cell calculated on an $8 \times 8 \times 8$ k grid and utilize Bloch eigenstates corresponding to the conduction band for e^- and the valence band for h^+. Transforming them to maximally localized Wannier functions within an $8 \times 8 \times 8$ supercell is achieved via WANNIER90. We neglect orbitals that do not strongly contribute to e^- and h^+ wave functions in this procedure; that is, we employ Pb p orbitals for e^- and Pb s as well as X p orbitals for h^+.

The Wannier functions for e^- or h^+ are then placed at different starting positions in the original $16 \times 16 \times 16$ supercell such that the initial wave function always starts evolving in the center of the periodically continued $96 \times 96 \times 96$ supercell. We propagate these initial wave functions via a product of time evolution operators, where each operator is constructed out of one Hamiltonian from the temporal series by a truncated Taylor expansion of the order of 50 with a time step of 1 fs. Further details on the time evolution can be found in Ref. [22]. From the time-evolved wave functions, we calculate the mean-square displacement (MSD) of charge carriers. Its diffusive part, averaged over different starting positions of the initial wave function in the crystal, yields e^- and h^+ mobilities via the Einstein-Smoluchowski relation. From this procedure, one can determine the carrier mobility at different temperatures [22,24].

III. RESULTS

In this study, we investigate the interplay between on-site energies, the magnitude of SOC, and carrier dynamics in $MAPbBr_3$ and $MAPbI_3$. To this end, we compute dynamic orbital populations and assess their role in electronic transport phenomena via a real-space analysis of carrier scattering.

A. Initial wave functions localized at single orbitals

We start our investigation by calculating the dynamic evolution of wave functions localized at an individual orbital that contributes to band-edge states of $MAPbI_3$ and $MAPbBr_3$. These orbitals are the Pb s, Pb p, X $p\sigma$, and X $p\pi$ orbitals. Here, X $p\pi$ refers to orbitals involved in $pp\pi$-hopping elements due to interactions between X p and Pb p states. Likewise, X $p\sigma$ corresponds to orbitals involved in $sp\sigma$- and $pp\sigma$-hopping elements. Figure 2 shows their MSDs resulting from an initial wave function localized at a single orbital on one atomic site for the two HaPs. Except for the X $p\pi$ orbitals, the MSDs can be separated into three regimes. First, the MSD rises sharply during ≈10 fs, reflecting a quick dispersal of the artificially localized initial wave function. Second, between roughly 10 and 35 fs, the MSDs show a quadratic increase in time; i.e., wave functions spread ballistically. Third, for times larger than ≈35 fs, we find a linear increase in the MSDs, and diffusive transport sets in.

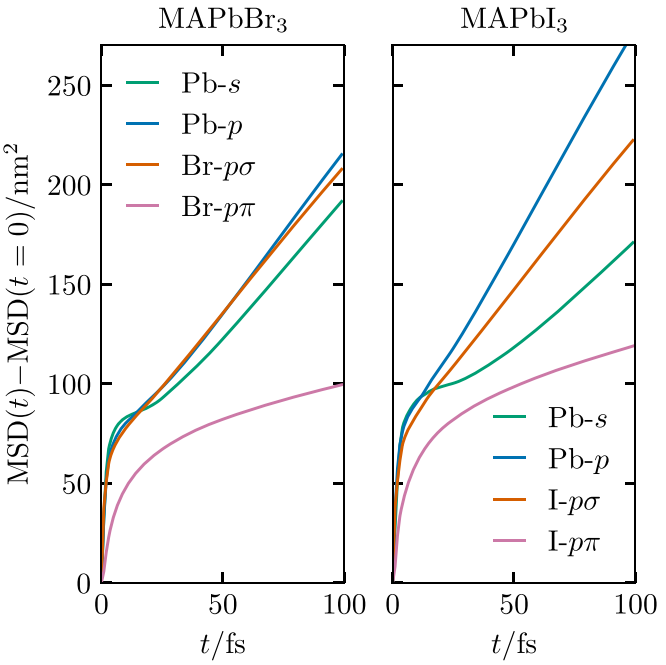


FIG. 2. Mean-square displacement of carrier wave functions initialized in either a Pb s, Pb p, X $p\sigma$, or X $p\pi$ orbital for $MAPbBr_3$ and $MAPbI_3$.

In contrast, the dispersal of X $p\pi$ orbitals does not follow this sequence and is strongly suppressed. We observe that MSDs for these orbitals saturate at a comparably low value in both materials, indicating that an entirely different transport mechanism is at play in this case. If we compare the transport behavior for the other orbital types, in the case of $MAPbBr_3$ the MSDs are close to each other, while for $MAPbI_3$ they are more spread out, with an enhanced Pb p and a suppressed Pb s curve. We conclude that the orbital configuration influences the transport mechanisms within the DD model, resulting in a different spread of the carrier wave function at early times of the system's quantum dynamics.

Figure 3 shows the population across different orbitals as a function of time proceeding the initialization of wave functions we showed in Fig. 2. We observe sharp changes among relative orbital occupations during the first few femtoseconds for all initialization scenarios. They correspond to the strong dispersal of the artificially localized initial wave functions seen at early times in the MSDs of Fig. 2. This behavior is

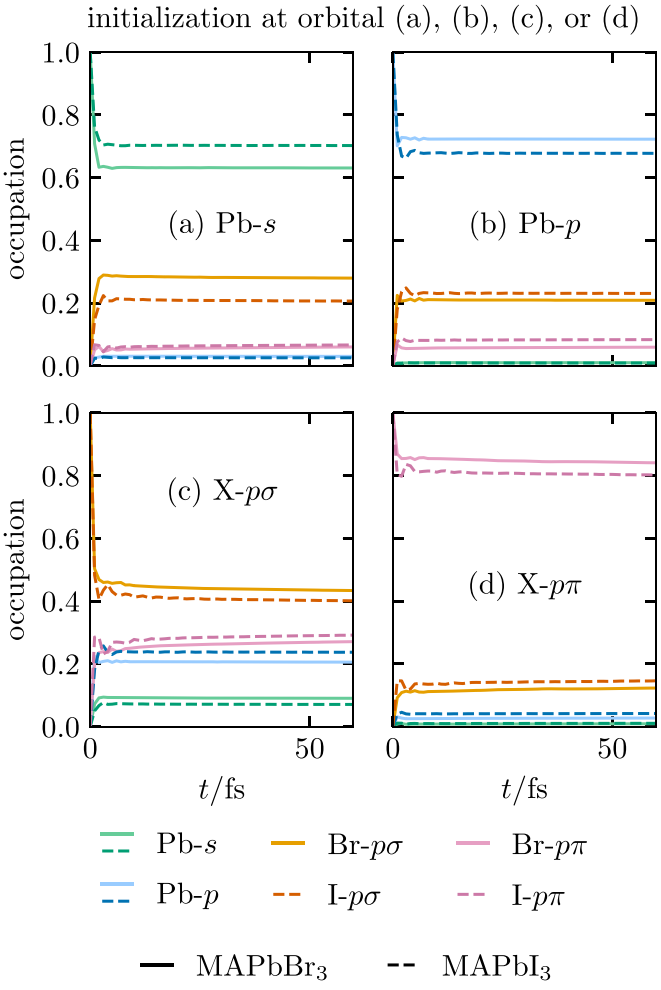


FIG. 3. Time evolution of the relative occupation for the orbital types Pb s, Pb p, X $p\sigma$, and X $p\pi$ in MAPbX_3 (X=Br, I) when different wave functions localized in a single orbital are used in the initialization (see Fig. 2). (a)–(d) correspond to an initial wave function localized in a single Pb s, Pb p, X $p\sigma$, and X $p\pi$ orbital, respectively.

followed by plateaus of relative orbital occupation in time when local fluctuations are averaged out. These stable orbital occupations reflect a balanced transport mechanism within the DD model, in which each orbital type steadily contributes to the overall charge conduction.

Like above, we observe differences depending on which orbital is used in the initialization of the wave functions: When a Pb s state is chosen in the initialization [see Fig. 3(a)], Pb s and X $p\sigma$ orbitals dominate the temporal charge carrier distribution. Notably, these orbital types are involved in $sp\sigma$ bonds. In contrast, when a Pb p state is used in the initialization [see Fig. 3(b)], charge carriers primarily occupy Pb p and X $p\sigma$ orbitals over time. These orbital types are involved in $pp\sigma$ bonds.

We rationalize the above findings using real-space transport channels that are visualized schematically in Fig. 4. Each channel corresponds to one of the three bond types, i.e., $sp\sigma$, $pp\sigma$, and $pp\pi$. In the DD model, charge carrier wave functions are transferred exclusively through the orbitals involved in these bonds, and hence, the channels collectively

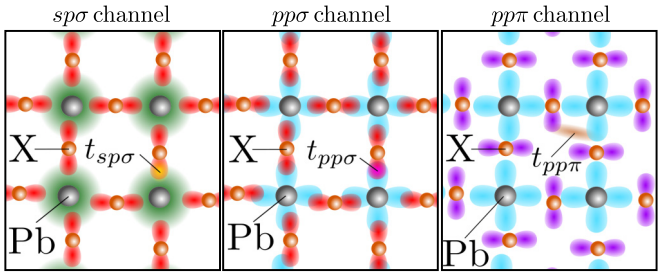


FIG. 4. Schematic visualization of the three transport channels, each driven by one of the TB hopping parameter types, $sp\sigma$, $pp\sigma$, and $pp\pi$. Pb ions are shown in gray, halides are in orange, Pb s orbitals are in green, Pb p orbitals are in blue, X $p\sigma$ orbitals are in red, and X $p\pi$ orbitals are in purple. For easy visualization, we show a two-dimensional slice of a cubic HaP structure without MA cations.

determine the charge carrier transport in HaPs. Revisiting the above results, in Fig. 3(a) only the $sp\sigma$ channel (Fig. 4, left panel) is active because only Pb s and X $p\sigma$ orbitals are significantly occupied. Likewise, in Fig. 3(b), the $pp\sigma$ channel (Fig. 4, middle panel) almost exclusively determines transport because mainly Pb p and X $p\sigma$ orbitals are occupied. However, a mixture of all channels occurs in Fig. 3(c) because the initial wave function localized at an X $p\sigma$ orbital connects both the $sp\sigma$ and $pp\sigma$ channels.

In contrast, Fig. 3(d) shows that carriers remain localized in X $p\pi$ orbitals. We compute the averages and standard deviations of all TB parameters along an MD trajectory of MAPbBr$_3$ and MAPbI$_3$ at 300 K and report them in Table I. Compared to $\bar{t}_{sp\sigma}$ and $\bar{t}_{pp\sigma}$, the hopping parameter $\bar{t}_{pp\pi}$ is significantly smaller. This can be understood by considering the reduced overlap of orbitals involved in the $pp\pi$ channel (Fig. 4, right panel). Consequently, the $pp\pi$ channel is a bottleneck channel for charge transport, which explains the reduced MSD we found when X $p\pi$ orbitals were used to initialize the wave function (see Fig. 2).

B. Full initial electron and hole wave functions

In this section, we analyze the temporal evolution of MSDs and relative orbital occupations using full e^- and

TABLE I. Mean values of on-site, hopping, and SOC parameters for MAPbBr$_3$ and MAPbI$_3$ at 300 K. The values are calculated by averaging all parameters of the same type within the Hamiltonian time series. We also report standard deviations for all parameters except the ones for SOC, which we have set to their mean values (see Sec. II).

	MAPbBr$_3$	MAPbI$_3$
$\bar{\varepsilon}^p_{\mathrm{Pb}}$ (eV)	3.23 ± 0.20	2.58 ± 0.20
$\bar{\varepsilon}^p_{\mathrm{X}}$ (eV)	-2.06 ± 0.25	-1.57 ± 0.23
$\bar{\varepsilon}^s_{\mathrm{Pb}}$ (eV)	-6.74 ± 0.20	-7.06 ± 0.19
$\bar{t}_{sp\sigma}$ (eV)	1.25 ± 0.28	1.12 ± 0.25
$\bar{t}_{pp\sigma}$ (eV)	2.01 ± 0.29	1.90 ± 0.26
$\bar{t}_{pp\pi}$ (eV)	0.48 ± 0.13	0.42 ± 0.12
$\bar{\gamma}_{\mathrm{X}}$ (eV)	0.165	0.323
$\bar{\gamma}_{\mathrm{Pb}}$ (eV)	0.538	0.520

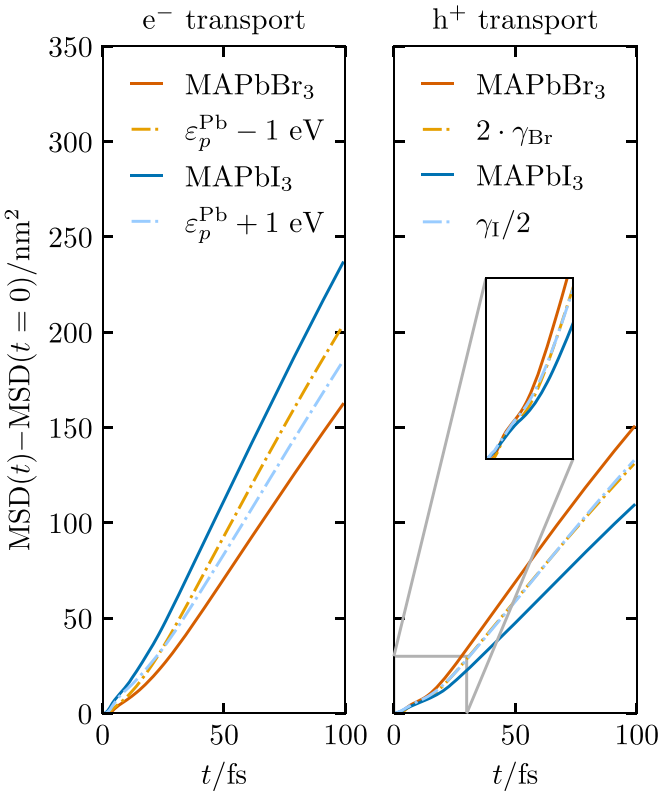


FIG. 5. MSDs for full initialization of electron (e^-, left) and hole (h^+, right) wave functions. Solid lines show the results of calculations performed as described in Sec. II without altering TB parameters. Dot-dashed lines show the results of calculations in which the TB parameters have been modified. The inset shows the MSD rise for the first 30 fs.

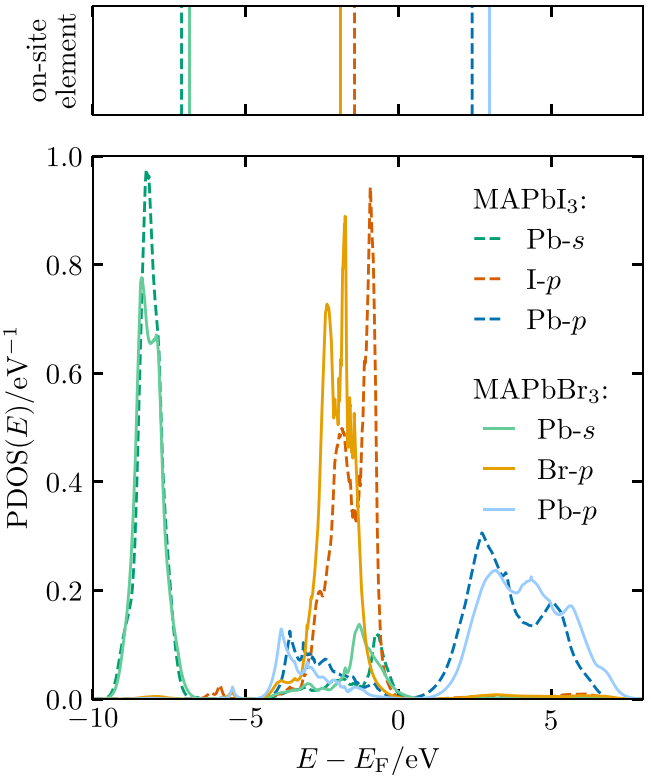


FIG. 6. Projected density of states (PDOS) for the orbital types Pb s, Pb p, and X p in $MAPbBr_3$ (solid lines) and $MAPbI_3$ (dashed lines). The eigenenergies were evaluated with DFT using a $2 \times 2 \times 2$ supercell and the HSE functional. We used WANNIER90 to calculate the PDOS and on-site level energies and set the Fermi energy E_F to the energy of the highest occupied state.

h^+ wave functions and apply the insights about real-space transport channels from above. Furthermore, we study how on-site levels and SOC affect the transport channels to explain differences between $MAPbBr_3$ and $MAPbI_3$. We further demonstrate a tuning of charge transport by adjusting on-site levels and SOC parameters.

Figure 5 shows the MSD over time for full initial e^- and h^+ wave functions (see Sec. II). Like above, the MSDs display three temporal regimes, beginning with a sharp rise, followed by a ballistic quadratic increase and a merging into a diffusive linear behavior. Compared to Fig. 2, the initial sharp rise is significantly less pronounced, owing to the more physical choice of initial wave functions, which can be seen in the inset of Fig. 5. For $MAPbBr_3$, the MSDs correspond to electron and hole mobilities of $\mu_e = 121\,\mathrm{cm}^2/\mathrm{V\,s}$ and $\mu_h = 113\,\mathrm{cm}^2/\mathrm{V\,s}$, while for $MAPbI_3$ they are $\mu_e = 171\,\mathrm{cm}^2/\mathrm{V\,s}$ and $\mu_h = 81\,\mathrm{cm}^2/\mathrm{V\,s}$. Experimental data on carrier mobilities of HaPs strongly depend on measurement and synthesis techniques [55,56]. While our calculated values are in the range of several previously reported experimental values, we note that, in contrast to our results, the experimentally reported h^+ mobilities are often larger than the e^- mobilities [56].

We explore the role of on-site energies in charge transport by modifying the TB parameters, shifting the on-site energy levels of Pb p orbitals ε_p^{Pb} for e^- transport (Fig. 5, left panel). We separately rescale the halide SOC strengths γ_X for h^+ transport (Fig. 5, right panel). Without these parameter changes, e^- transport is stronger than h^+ transport in both materials. Moreover, for e^- transport the MSD increases more strongly in $MAPbI_3$ compared to $MAPbBr_3$ and vice versa for h^+ transport. Exploring the origins of these observations, we find that modifying the Pb p on-site energy levels enhances the magnitude of the MSD for e^- when ε_p^{Pb} is lowered, while raising ε_p^{Pb} has the opposite effect. We observe complementary effects for adjusting the halide onsite levels ε_p^X such that a smaller gap between the two levels, ε_p^{Pb} and ε_p^X, always intensifies the overall transport, while a larger gap weakens it. In contrast, altering the on-site energy levels of Pb s orbitals ε_s^{Pb} barely influences the e^- transport. However, for h^+ transport, reducing and increasing ε_p^{Pb} raise the MSD magnitude by similar amounts [54]. Meanwhile, an increased (decreased) halide SOC strength γ_X suppresses (enhances) the magnitude of the MSD for h^+ transport, whereas rescaling γ_X has almost no impact on e^- transport.

To rationalize the consequences of the parameter changes on the transport results, we link the TB model to the more intuitive projected density of states (PDOS) and illustrate the impact of level shifts on the electronic structure. Therefore, we use DFT to calculate the PDOS of $MAPbBr_3$ and $MAPbI_3$ for the three orbitals types, Pb s, Pb p, and X p, at one representative atomic site for a randomly selected snapshot along the MD trajectory (Fig. 6, bottom panel) and calculate

their corresponding on-site energy levels (Fig. 6, top panel). Although the shown PDOS reflects the electronic structure of merely one structural configuration, the following findings hold because the dominant features of the PDOS remain consistent across MD snapshots even when there are temporal changes in on-site levels and energy gaps. As has been well established for these materials [57,58], Pb p orbitals dominate the conduction band, while the valence band shows contributions from all orbital types, with X p orbitals being most prominent. It is also well-known that the fundamental band gap of $MAPbI_3$ is smaller than that of $MAPbBr_3$ [52]. This is also reflected in their on-site level structure since on-site levels match the main weights of their corresponding PDOS. Moreover, the PDOS relates analytically to the energy of the on-site energy levels via

$$\varepsilon_\alpha^i = \int_{-\infty}^{\infty} \varepsilon \times \mathrm{PDOS}_\alpha^i(\varepsilon)\, \mathrm{d}\varepsilon. \tag{1}$$

This relation directly connects $\mathrm{PDOS}_\alpha^i(\varepsilon)$, which is the PDOS of an orbital α at site i, to the respective on-site energy ε_α^i. Likewise, the crystal orbital bond index (COBI) [59] is related to the hopping elements [54]. Together, the PDOS and the COBI offer an easy-to-follow framework for interpreting the impact of changes in the TB parametrization on the electronic structure.

To further investigate the parameter adjustments shown in Fig. 5, we analyze the relative orbital occupation over time in Fig. 7 for e^- and h^+ wave functions that are fully initialized according to the Bloch eigenstates of conduction and valence band states. We probe the role of the transport channels described above in realistic carrier-scattering scenarios and determine how shifts of on-site levels and halide SOC magnitude impact transport.

The top panels of Fig. 7 show the relative orbital occupations for initial e^- wave functions with and without introducing shifts for $\varepsilon_p^{\mathrm{Pb}}$ (see Fig. 5, left panel). In both HaPs, initial e^- wave functions are mostly composed of orbitals that make up the conduction band states; i.e., they show dominant Pb p contributions (see Fig. 6). These orbitals remain the primary contributors over time, whereas the Pb s orbitals remain weakly occupied. Since the Pb s orbital is essential in the composition of the $sp\sigma$ channel, the lack of its occupation indicates that the $sp\sigma$ channel is irrelevant in the case of e^- transport. Thus, on-site level shifts for Pb s orbitals do not affect e^- transport as described above. However, level shifts for Pb p orbitals have a noticeable effect: When we apply shifts that align the Pb p on-site levels for the two HaPs more (see Table I), we find the relative occupations between $MAPbBr_3$ and $MAPbI_3$ become more similar too. This is also reflected in the occupation of Pb p levels being closer to X $p\sigma$ and X $p\pi$ orbitals when we reduce the energy level of Pb p, as shown in the top left panel of Fig. 7.

The on-site level shifts and related changes in the occupations influence the transport strength through the following mechanism. When we shift two on-site energy levels involved in a transport channel toward each other, their occupations also become slightly more aligned. This more balanced charge distribution among the two involved orbital types implies a steadier flow of the carrier wave function and thereby leads to enhanced carrier transport along this channel.

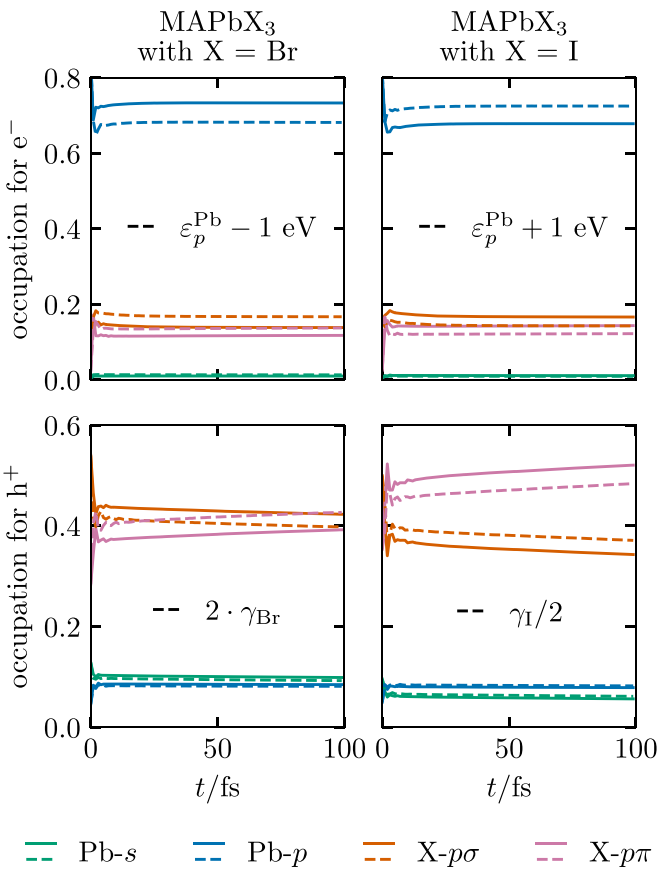


FIG. 7. Time evolution of the relative occupation for the orbital types Pb s, Pb p, X $p\sigma$, and X $p\pi$ in $MAPbX_3$ (X=Br, I) when full initial electron (e^-, top panels) and hole (h^+, bottom panels) wave functions are used in the initialization (see Fig. 5). Each subplot reflects the parameter change specified in its legend.

In essence, a smaller energy gap between the Pb p and halide on-site levels facilitates level transitions and therefore stronger transport along the $pp\sigma$ channel, which is consistent with our observations (see Fig. 5, left panel). The stimulation of transitions by level shifts found here is reminiscent of the proportionality between the transition probability and energy level difference for Rabi cycles, which can be analytically shown for a two-level system [60]. The same principles apply when we introduce on-site level shifts for X p orbitals. Accordingly, the differences in X p and Pb p on-site level gaps between the two HaPs partly account for the higher MSD for $MAPbI_3$ compared to $MAPbBr_3$ in the case of e^- transport. The residual difference in their MSDs, even after aligning the on-site level structure, then predominantly stems from the variation in the strengths and DD of the hopping parameters (see Table I). We note in passing that the interplay between level gaps we describe here is different from the impact of varying the Holstein electron-phonon coupling, even though it can also manifest in shifts of the on-site levels [61], and is also different from the influence of the DD originating from the on-site elements [45]. We further note that $MASnI_3$ shows a narrower on-site level gap between I p and metal cation p orbitals [62] compared to $MAPbI_3$, which could at least partly explain the generally larger carrier mobilities of $MASnI_3$ compared to $MAPbI_3$ [55].

The bottom panels of Fig. 7 show relative orbital occupations for initial h^+ wave functions with and without rescaling of γ_X (see Fig. 5, right panel). In both HaPs, X p states are the strongest contributing orbital types owing to their large weights in the valence band states (see Fig. 6). Since X p orbitals participate in every channel, a mixture of all three channels occurs in the case of h^+ transport. Hence, the bottleneck, $pp\pi$ channel also plays an active role in the case of h^+ transport and weakens it. This can be assessed by comparing the magnitude of the X $p\pi$ orbital occupation for h^+ and e^-, which in the case of the latter is much less pronounced and, thus, the suppressing nature of the $pp\pi$ channel is substantially less relevant.

Comparing the two HaPs for the case of h^+ transport, a stronger occupation of X $p\pi$ orbitals for $MAPbI_3$ than for $MAPbBr_3$ entails a more dominant role of the $pp\pi$ channel, which impedes transport. Figure 7 shows that the occupation of X $p\pi$ orbitals is impacted by the magnitude of γ_X, which can be interpreted as an additional hopping term between X $p\pi$ and X $p\sigma$ orbitals within our TB model. As indicated by the bottom panels of Fig. 7, increasing γ_X increases the occupation of X $p\pi$ orbitals and suppresses transport. For the same reason, e^- transport is unaffected by γ_X because the occupation of X $p\pi$ is negligible in this case [54]. Since halide SOC parameters of $MAPbI_3$ are approximately twice as large as that of $MAPbBr_3$ (see Table I), the difference in the γ_X parameters partly explains their MSD difference. Thus, the predicted higher h^+ mobility in $MAPbBr_3$ compared to $MAPbI_3$ (see Fig. 5, right panel), which agrees with experimentally observed trends [55,56], can in part be attributed to the stronger SOC in the case of iodide.

IV. CONCLUSIONS

In summary, this work investigated charge carrier transport in two prototypical HaP materials, namely, $MAPbBr_3$ and $MAPbI_3$. We used and further developed the DD model with a focus on the choice of electronic-structure theory and real-space charge transport channels. Investigating the temporal behaviors of orbital occupations, we examined the consequences of on-site energy levels and the strength of SOC, which are determined by the chemical composition of the material. We found that both on-site energies and the magnitude of SOC influence the relative orbital occupations and, with that, the dispersal of charge and carrier transport. Specifically, the energy gaps emerging across the on-site levels determine to what extent the charge transport channels get filled over time. Identifying the $pp\pi$ channel as a bottleneck for charge transport, we were able to rationalize differences between e^- and h^+ transport and explain different characteristics of the two investigated materials. Altogether, the present study demonstrates the capabilities of a real-space analysis for the carrier dynamics in HaPs and motivates further development of related concepts for other material families.

ACKNOWLEDGMENTS

Funding provided by Germany's Excellence Strategy – EXC 2089/1-390776260, by the Deutsche Forschungsgemeinschaft (DFG) via SPP2196 Priority Program (Project ID No. 424709454), and by the Studienstiftung des Deutschen Volkes is gratefully acknowledged. The authors further acknowledge the Gauss Centre for Supercomputing e.V. for funding this project by providing computing time through the John von Neumann Institute for Computing on the GCS Supercomputer JUWELS at Jülich Supercomputing Centre.

DATA AVAILABILITY

The data that support the findings of this article are openly available [63].

[1] S. D. Stranks and H. J. Snaith, Metal-halide perovskites for photovoltaic and light-emitting devices, Nat. Nanotechnol. **10**, 391 (2015).

[2] J.-P. Correa-Baena, M. Saliba, T. Buonassisi, M. Grätzel, A. Abate, W. Tress, and A. Hagfeldt, Promises and challenges of perovskite solar cells, Science **358**, 739 (2017).

[3] J. Liu, J. Qu, T. Kirchartz, and J. Song, Optoelectronic devices based on the integration of halide perovskites with silicon-based materials, J. Mater. Chem. A **9**, 20919 (2021).

[4] T. M. Brenner, D. A. Egger, L. Kronik, G. Hodes, and D. Cahen, Hybrid organic–inorganic perovskites: low-cost semiconductors with intriguing charge-transport properties, Nat. Rev. Mater. **1**, 15007 (2016).

[5] J. S. Manser, J. A. Christians, and P. V. Kamat, Intriguing optoelectronic properties of metal halide perovskites, Chem. Rev. **116**, 12956 (2016).

[6] C. C. Stoumpos and M. G. Kanatzidis, Halide perovskites: Poor man's high-performance semiconductors, Adv. Mater. **28**, 5778 (2016).

[7] W. Li, Z. Wang, F. Deschler, S. Gao, R. H. Friend, and A. K. Cheetham, Chemically diverse and multifunctional hybrid organic–inorganic perovskites, Nat. Rev. Mater. **2**, 2058 (2017).

[8] S. De Wolf, J. Holovsky, S.-J. Moon, P. Löper, B. Niesen, M. Ledinsky, F.-J. Haug, J.-H. Yum, and C. Ballif, Organometallic halide perovskites: Sharp optical absorption edge and its relation to photovoltaic performance, J. Phys. Chem. Lett. **5**, 1035 (2014).

[9] M. Baranowski and P. Plochocka, Excitons in metal-halide perovskites, Adv. Energy Mater. **10**, 1903659 (2020).

[10] S. D. Stranks, G. E. Eperon, G. Grancini, C. Menelaou, M. J. P. Alcocer, T. Leijtens, L. M. Herz, A. Petrozza, and H. J. Snaith, Electron-hole diffusion lengths exceeding 1 micrometer in an organometal trihalide perovskite absorber, Science **342**, 341 (2013).

[11] M. B. Johnston and L. M. Herz, Hybrid perovskites for photovoltaics: Charge-carrier recombination, diffusion, and radiative efficiencies, Acc. Chem. Res. **49**, 146 (2016).

[12] E. L. Unger, L. Kegelmann, K. Suchan, D. Sörell, L. Korte, and S. Albrecht, Roadmap and roadblocks for the band gap tunability of metal halide perovskites, J. Mater. Chem. A **5**, 11401 (2017).

[13] P. Y. Yu and M. Cardona, *Fundamentals of Semiconductors* (Springer, Berlin, 2010).

[14] M. J. Schilcher, P. J. Robinson, D. J. Abramovitch, L. Z. Tan, A. M. Rappe, D. R. Reichman, and D. A. Egger, The significance of polarons and dynamic disorder in halide perovskites, ACS Energy Lett. **6**, 2162 (2021).

[15] A. Troisi and G. Orlandi, Charge-transport regime of crystalline organic semiconductors: Diffusion limited by thermal off-diagonal electronic disorder, Phys. Rev. Lett. **96**, 086601 (2006).

[16] S. Fratini and S. Ciuchi, Bandlike motion and mobility saturation in organic molecular semiconductors, Phys. Rev. Lett. **103**, 266601 (2009).

[17] A. S. Mishchenko, L. Pollet, N. V. Prokof'ev, A. Kumar, D. L. Maslov, and N. Nagaosa, Polaron mobility in the "beyond quasiparticles" regime, Phys. Rev. Lett. **123**, 076601 (2019).

[18] S. Giannini, O. G. Ziogos, A. Carof, M. Ellis, and J. Blumberger, Flickering polarons extending over ten nanometres mediate charge transport in high-mobility organic crystals, Adv. Theory Simul. **3**, 2000093 (2020).

[19] C. Quarti, E. Mosconi, J. M. Ball, V. D'Innocenzo, C. Tao, S. Pathak, H. J. Snaith, A. Petrozza, and F. De Angelis, Structural and optical properties of methylammonium lead iodide across the tetragonal to cubic phase transition: implications for perovskite solar cells, Energy Environ. Sci. **9**, 155 (2016).

[20] O. Yaffe, Y. Guo, L. Z. Tan, D. A. Egger, T. Hull, C. C. Stoumpos, F. Zheng, T. F. Heinz, L. Kronik, M. G. Kanatzidis, J. S. Owen, A. M. Rappe, M. A. Pimenta, and L. E. Brus, Local polar fluctuations in lead halide perovskite crystals, Phys. Rev. Lett. **118**, 136001 (2017).

[21] A. Marronnier, G. Roma, S. Boyer-Richard, L. Pedesseau, J.-M. Jancu, Y. Bonnassieux, C. Katan, C. C. Stoumpos, M. G. Kanatzidis, and J. Even, Anharmonicity and disorder in the black phases of cesium lead iodide used for stable inorganic perovskite solar cells, ACS Nano **12**, 3477 (2018).

[22] M. Z. Mayers, L. Z. Tan, D. A. Egger, A. M. Rappe, and D. R. Reichman, How lattice and charge fluctuations control carrier dynamics in halide perovskites, Nano Lett. **18**, 8041 (2018).

[23] C. Gehrmann and D. A. Egger, Dynamic shortening of disorder potentials in anharmonic halide perovskites, Nat. Commun. **10**, 3141 (2019).

[24] M. J. Schilcher, D. J. Abramovitch, M. Z. Mayers, L. Z. Tan, D. R. Reichman, and D. A. Egger, Correlated anharmonicity and dynamic disorder control carrier transport in halide perovskites, Phys. Rev. Mater. **7**, L081601 (2023).

[25] S. A. Seidl, X. Zhu, G. Reuveni, S. Aharon, C. Gehrmann, Sebastián Caicedo-Dávila, O. Yaffe, and D. A. Egger, Anharmonic fluctuations govern the band gap of halide perovskites, Phys. Rev. Mater. **7**, L092401 (2023).

[26] M. Zacharias, G. Volonakis, F. Giustino, and J. Even, Anharmonic electron-phonon coupling in ultrasoft and locally disordered perovskites, npj Comput. Mater. **9**, 153 (2023).

[27] M. Frenzel, M. Cherasse, J. M. Urban, F. Wang, B. Xiang, L. Nest, L. Huber, L. Perfetti, M. Wolf, T. Kampfrath, X.-Y. Zhu, and S. F. Maehrlein, Nonlinear terahertz control of the lead halide perovskite lattice, Sci. Adv. **9**, eadg3856 (2023).

[28] Y. Park and D. T. Limmer, Biexcitons are bound in $CsPbBr_3$ perovskite nanocrystals, Phys. Rev. Mater. **7**, 106002 (2023).

[29] J. Wiktor, E. Fransson, D. Kubicki, and P. Erhart, Quantifying dynamic tilting in halide perovskites: Chemical trends and local correlations, Chem. Mater. **35**, 6737 (2023).

[30] C. M. Hylton-Farrington and R. C. Remsing, Dynamic local symmetry fluctuations of electron density in halide perovskites, Chem. Mater. **36**, 9442 (2024).

[31] X. Zhu and D. A. Egger, Effect of overdamped phonons on the fundamental band gap of perovskites, Phys. Rev. Lett. **134**, 016403 (2025).

[32] A. F. Ioffe and A. R. Regel, Non-crystalline, amorphous, and liquid electronic semiconductors, Prog. Semicond. **4**, 237 (1960).

[33] N. Mott, *Metal-Insulator Tranisitions* (CRC Press, Boca Raton, FL, 1990).

[34] J. Wiktor, I. Reshetnyak, F. Ambrosio, and A. Pasquarello, Comprehensive modeling of the band gap and absorption spectrum of $BiVO_4$, Phys. Rev. Mater. **1**, 022401(R) (2017).

[35] J.-J. Zhou and M. Bernardi, Predicting charge transport in the presence of polarons: The beyond-quasiparticle regime in $SrTiO_3$, Phys. Rev. Res. **1**, 033138 (2019).

[36] F. S. Hegner, A. Cohen, S. S. Rudel, S. M. Kronawitter, M. Grumet, X. Zhu, R. Korobko, L. Houben, C.-M. Jiang, W. Schnick, G. Kieslich, O. Yaffe, I. D. Sharp, and D. A. Egger, The critical role of anharmonic lattice dynamics for macroscopic properties of the visible light absorbing nitride semiconductor $CuTaN_2$, Adv. Energy Mater. **14**, 2303059 (2024).

[37] L. Wang, D. Beljonne, L. Chen, and Q. Shi, Mixed quantum-classical simulations of charge transport in organic materials: Numerical benchmark of the Su-Schrieffer-Heeger model, J. Chem. Phys. **134**, 244116 (2011).

[38] A. Troisi, Charge transport in high mobility molecular semiconductors: classical models and new theories, Chem. Soc. Rev. **40**, 2347 (2011).

[39] S. Ciuchi and S. Fratini, Electronic transport and quantum localization effects in organic semiconductors, Phys. Rev. B **86**, 245201 (2012).

[40] S. Fratini, D. Mayou, and S. Ciuchi, The transient localization scenario for charge transport in crystalline organic materials, Adv. Funct. Mater. **26**, 2292 (2016).

[41] H. Oberhofer, K. Reuter, and J. Blumberger, Charge transport in molecular materials: An assessment of computational methods, Chem. Rev. **117**, 10319 (2017).

[42] S. Giannini, A. Carof, M. Ellis, H. Yang, O. G. Ziogos, S. Ghosh, and J. Blumberger, Quantum localization and delocalization of charge carriers in organic semiconducting crystals, Nat. Commun. **10**, 3843 (2019).

[43] M. Asher, D. Angerer, R. Korobko, Y. Diskin-Posner, D. A. Egger, and O. Yaffe, Anharmonic lattice vibrations in small-molecule organic semiconductors, Adv. Mater. **32**, 1908028 (2020).

[44] S. Giannini, L. Di Virgilio, M. Bardini, J. Hausch, J. J. Geuchies, W. Zheng, M. Volpi, J. Elsner, K. Broch, Y. H. Geerts, F. Schreiber, G. Schweicher, H. I. Wang, J. Blumberger, M. Bonn, and D. Beljonne, Transiently delocalized states enhance hole mobility in organic molecular semiconductors, Nat. Mater. **22**, 1361 (2023).

[45] A. Lacroix, G. T. de Laissardière, P. Quémerais, J.-P. Julien, and D. Mayou, Modeling of electronic mobilities in halide perovskites: Adiabatic quantum localization scenario, Phys. Rev. Lett. **124**, 196601 (2020).

[46] P. Dörflinger, P. Rieder, and V. Dyakonov, Temperature-dependent charge-carrier dynamics in lead-halide perovskites:

Indications for dynamic disorder dominated scattering mechanism, Adv. Energy Mater. **15**, 2403332 (2025).

[47] G. Kresse and J. Furthmüller, Efficient iterative schemes for *ab initio* total-energy calculations using a plane-wave basis set, Phys. Rev. B **54**, 11169 (1996).

[48] J. Heyd, G. E. Scuseria, and M. Ernzerhof, Hybrid functionals based on a screened Coulomb potential, Chem. Phys. **118**, 8207 (2003).

[49] J. Heyd, G. E. Scuseria, and M. Ernzerhof, Erratum: "Hybrid functionals based on a screened Coulomb potential" [J. Chem. Phys. 118, 8207 (2003)], J. Chem. Phys. **124**, 219906 (2006).

[50] J. P. Perdew, K. Burke, and M. Ernzerhof, Generalized gradient approximation made simple, Phys. Rev. Lett. **77**, 3865 (1996).

[51] Y. Yuan, R. Xu, H.-T. Xu, F. Hong, F. Xu, and L.-J. Wang, Nature of the band gap of halide perovskites ABX_3($A = CH_3NH_3$, Cs; B = Sn, Pb; X = Cl, Br, I): First-principles calculations, Chin. Phys. B **24**, 116302 (2015).

[52] T. Das, G. Di Liberto, and G. Pacchioni, Density functional theory estimate of halide perovskite band gap: When spin orbit coupling helps, J. Phys. Chem. C **126**, 2184 (2022).

[53] G. Pizzi, V. Vitale, R. Arita, S. Blügel, F. Freimuth, G. Géranton, M. Gibertini, D. Gresch, C. Johnson, T. Koretsune *et al.*, Wannier90 as a community code: new features and applications, J. Phys.: Condens. Matter **32**, 165902 (2020).

[54] See Supplemental Material at http://link.aps.org/supplemental/10.1103/c4v6-kf43 for more details on the impact of the functional on the hopping elements, additional results for the influence of the number of MD snapshots on tight-binding parameter estimation, and the connection of the crystal orbital bond index to the hopping elements.

[55] L. M. Herz, Charge-carrier mobilities in metal halide perovskites: Fundamental mechanisms and limits, ACS Energy Lett. **2**, 1539 (2017).

[56] A. Capitaine and B. Sciacca, Monocrystalline methylammonium lead halide perovskite materials for photovoltaics, Adv. Mater. **33**, 2102588 (2021).

[57] S. Ashhab, O. Voznyy, S. Hoogland, E. H. Sargent, and M. E. Madjet, Effect of disorder on transport properties in a tight-binding model for lead halide perovskites, Sci. Rep. **7**, 8902 (2017).

[58] A. Mehdizadeh, S. F. Akhtarianfar, and S. Shojaei, Role of methylammonium rotation in hybrid halide $MAPbX_3$ (X = I, Br, and Cl) perovskites by a density functional theory approach: Optical and electronic properties, J. Phys. Chem. C **123**, 6725 (2019).

[59] P. C. Müller, C. Ertural, J. Hempelmann, and R. Dronskowski, Crystal orbital bond index: Covalent bond orders in solids, J. Phys. Chem. C **125**, 7959 (2021).

[60] P. W. Atkins and R. S. Friedman, *Molecular Quantum Mechanics* (Oxford University Press, Oxford, 2005).

[61] J. H. Fetherolf, D. Golež, and T. C. Berkelbach, A unification of the Holstein polaron and dynamic disorder pictures of charge transport in organic crystals, Phys. Rev. X **10**, 021062 (2020).

[62] C. Paschal, A. Pogrebnoi, and T. Pogrebnaya, Guanidinium tin halide perovskites: structural, electronic, and thermodynamic properties by quantum chemical study, Appl. Phys. A **127**, 355 (2021).

[63] F. Vonhoff, M. J. Schilcher, D. R. Reichman, and D. A. Egger, Data for "Analysis of real-space transport channels for electrons and holes in halide perovskites," Zenodo (2025), https://zenodo.org/records/15855333.